

Article

Switchable Dual-Functional Metasurface for THz Absorption and Electromagnetically Induced Transparency

Haocheng Cai ^{1,†}, Yue Yang ^{2,†}, Jianchen Zi ³, Luhong Mao ¹ and Jining Li ^{4,*} ¹ School of Electrical and Information Engineering, Tianjin University, Tianjin 300072, China² School of Computer and Information Engineering, Tianjin Chengjian University, Tianjin 300384, China³ Jihua Laboratory, Foshan 528200, China⁴ Laboratory of Opto-Electronics Information Technology (Tianjin University), School of Precision Instruments and Opto-Electronics Engineering, Tianjin University, Ministry of Education, Tianjin 300072, China

* Correspondence: jiningli@tju.edu.cn

† These authors contributed equally to this work.

Abstract: The metasurfaces based on nanostructure film play an important role in many fields. Usually, the properties and functions of metasurfaces are limited by their structure. Once the metasurface samples are processed, their functions have already been restricted. The dual-function device designed in this work utilizes the phase transition characteristic of vanadium dioxide (VO₂). The entire layer of VO₂ film is inserted between the double metal micro-nano structure. When VO₂ film is in the metallic state after phase change, an isotropic narrow absorber is obtained in the terahertz (THz) region, which consists of a top Z-shaped meta-atom, a middle dielectric layer, and a bottom VO₂ film. By adjusting structure parameters of VO₂ film, perfect absorption is realized at the frequency of 0.525 THz with the overall absorption beyond 91%. When VO₂ is in insulating state, the top Z-shaped meta-atom will interact with the bottom Z-shaped structure, and the resonance coupling leads to the appearance of electromagnetically induced transparency (EIT). The designed metal-VO₂ hybrid metamaterial opens possible avenues for switchable functionalities in a single device.

Keywords: terahertz; VO₂; absorber; electromagnetic induced transparency; dual-functional



Citation: Cai, H.; Yang, Y.; Zi, J.; Mao, L.; Li, J. Switchable Dual-Functional Metasurface for THz Absorption and Electromagnetically Induced Transparency. *Coatings* **2023**, *13*, 816. <https://doi.org/10.3390/coatings13050816>

Academic Editor: Torsten Brezesinski

Received: 22 March 2023

Revised: 12 April 2023

Accepted: 16 April 2023

Published: 23 April 2023



Copyright: © 2023 by the authors. Licensee MDPI, Basel, Switzerland. This article is an open access article distributed under the terms and conditions of the Creative Commons Attribution (CC BY) license (<https://creativecommons.org/licenses/by/4.0/>).

1. Introduction

Diversification of optical system functions will greatly increase the complexity of itself, such as the bigger size, insertion loss, and economic cost. And the increase of elements will lead to an increase in optical distortion, system noise and measurement error. Integrating multiple modulation modes and functions into one device can provide new ideas. It can not only realize the diversity of functions, but also reduce the loss of the optical system. Metasurfaces are artificial micro-nano devices composed of a large number of periodic or non-periodic sub-wavelength structures arranged on a two-dimensional plane, which can deal with electromagnetic waves flexibly and realize many functions of traditional optical elements [1]. To realize the dynamic adjustment of the metasurface performance, the metasurface with phase change materials, Dirac semimetals, and graphene have been researched [1–3]. However, most active control metasurfaces have been reported as single-function devices, such as frequency control [4], filtering [5], or absorption [6,7]. There are few metasurfaces with more than two modulation modes or functions.

Vanadium dioxide (VO₂) is a typical phase change material that exhibits a transition from an insulating dielectric state to a conducting metal state at a critical temperature of around 340 K, which plays a great role in the modulation of terahertz metasurfaces [8–14]. VO₂ has advantages of the fast response [15], large modulation depth, and multiple modulation methods [16], such as optical pumping [17], thermal control [10,18] and extra electric fields [19,20]. It should be noted that VO₂ in the air is easy to spontaneously oxidize into

a more thermodynamically stable Vanadium pentoxide (V_2O_5), resulting in lost modulation characteristics. In practical applications, it is necessary to design an anti-reflection layer to block large area contact between VO_2 and oxygen in the air [21,22]. In recent years, there have been many reports on the regulation of metasurface properties by VO_2 materials. Most of the studies focus on the regulation of single function devices [23–26], while a few studies achieve multifunctional regulation [12,27,28]. Song et al. presented the bifunctional design of a broadband absorber and a broadband polarization converter [12]. Ding et al. proposed a metasurface switch between a wideband absorber and a reflective half wave plate [27]. Relevant applications include metamaterial absorber [29] realized in visible and near infrared bands, upper material photoluminescence forming absorber [30], absorption transmission measurement in closed environment [31] and nano-imprinted metasurface [32]. However, some proposed structure neglect to protect the VO_2 materials from oxidation [12,26–28]. Also, some proposed structures [12,23–28] are relatively complex and hard to process. Similar optical systems have shown some possibilities for global environmental issues: photocatalyst [33], photocatalysis and subsequent decontamination [34], and light absorption after photocatalytic removal of nitric oxide (NO) [35].

The metamaterial absorber uses electromagnetic resonance to achieve impedance matching at the air-metamaterial interface, which almost completely absorbs the electromagnetic wave near the resonance frequency. Thus, the entire incident energy is limited to the metamaterial reflector, which means that reflection is minimal, as opposed to absorption. Therefore, due to the limitation of electromagnetic field energy in the metamaterial absorber [36], approximately zero reflection and absorption efficiency greater than 90% are achieved, with excellent performance such as flexible design and wide band. Tunable terahertz absorbers with active materials, such as graphene, vanadium dioxide, or other conductive oxides [37–39]. On the other hand, electromagnetic induced transparency (EIT) is a kind of abnormal transmission phenomenon based on mode coupling, which has great application potential in slow light effect and electromagnetic modulation [40–43]. Metasurface based on vanadium dioxide-metal composite structure has achieved the switchable EIT phenomenon. However, there is little reported work on combining the two functions, with the active material in these devices acting as a switch to turn a single function on and off. The integration of metasurfaces with a full range of functions over a wide band and the integration of absorption-transmission regulation of a single device has not been realized, thus limiting their potential applications to meet the demand for multifunctional electromagnetic device integration and high capacity and speed operation.

In this paper, we propose a dual function control device. The narrow-band absorption function and the electromagnetically induced transparency effect are integrated into the same metasurface, which realizes the flexible switching of two functions in one device. When VO_2 is in the insulating state, the device will appear the electromagnetic induced transparency. When VO_2 is in the metallic state, the device will show relatively perfect narrow-band absorption. Meanwhile, our design avoids the large area of contact between VO_2 and air, thus protecting VO_2 from oxidation. Besides, we can use the same mask plate to complete the processing of the upper and lower Z-shaped structures, thus saving the cost of production. This dual-functional metasurface promises great application prospects in terahertz field.

2. Methods

2.1. Structure Design

The structure and parameters of the metasurface designed in this work are shown in Figure 1, which consists of five layers. As shown in Figure 1a, the unit cell of the metasurface consists of a top Z-shaped enantiomeric meta-atom, a top dielectric layer, a vanadium dioxide film, a bottom symmetric Z structure and a bottom dielectric spacer (SiO_2). Figure 1b,c show the side and top views of a unit cell of the structure, respectively. The thickness of the Au, top SiO_2 , VO_2 , bottom SiO_2 are $t_4 = 200$ nm, $t_3 = 15$ μ m, $t_2 = 0.5$ μ m, and $t_1 = 10$ μ m. The geometrical parameters of the unit cell, shown in Figure 1c, are set as

follows: $P = 200 \mu\text{m}$, $P_1 = 150 \mu\text{m}$, and $w = 15 \mu\text{m}$. The two layers of metal in the structure are made from the same Z-pattern through two lithographic processes. The preparation cost is greatly reduced by adopting the same Z mask version. This provides the possibility for large-scale industrial preparation.

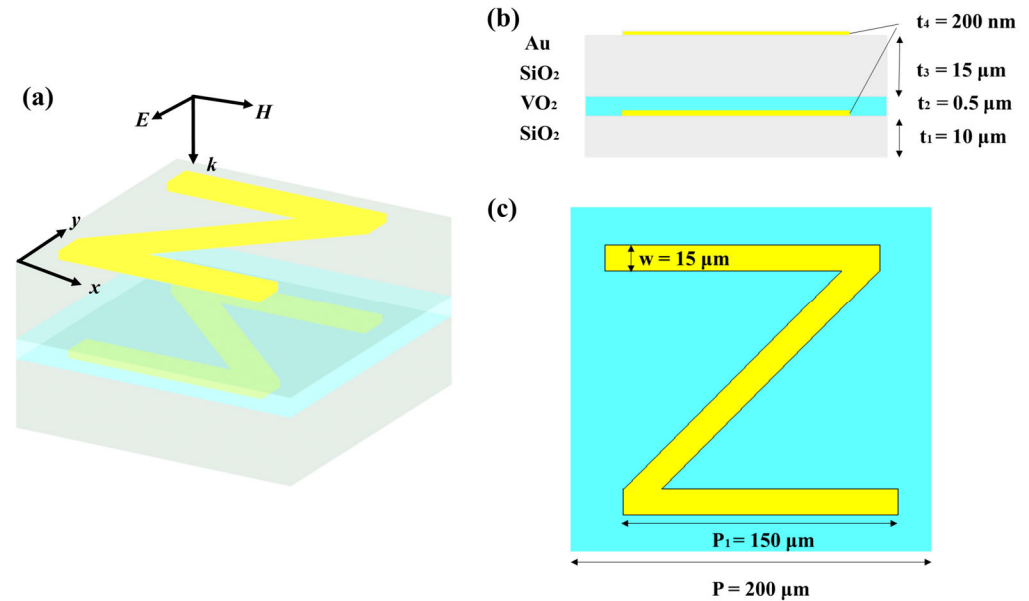


Figure 1. (a) Schematic of the unit cell of the dual-functional metasurface. (b) Side view and parameters. (c) The top view and parameters.

2.2. Characterization

The numerical simulations were conducted using finite element methods in the frequency-domain. Unit cell boundary conditions were considered both in the x , y and z directions. The SiO_2 was modeled as a lossless dielectric with a permittivity of $\epsilon = 3.8$, while the Au structure was modeled as a lossy metal with a conductivity of $\sigma = 4.56 \times 10^7 \text{ S/m}$. The optical properties of VO_2 in THz range is described by the Drude model [23,44,45], which is expressed by $\epsilon(\omega) = \epsilon' + i\epsilon'' = \epsilon_\infty - \frac{\omega_p^2(\sigma)}{\omega^2 + i\gamma\omega}$, where ϵ' represents the real part of the dielectric constant, i is an imaginary unit, which usually represents the strength of the material's polarization with the external electric field. ϵ'' represents the real part of the dielectric constant, which usually represents the loss of the material. In the expansion formula, ϵ_∞ represents the maximum dielectric constant of the material under the high order limiting electromagnetic wave frequency. Within the range of THz, the value of this limiting dielectric constant is 12. γ representing the permittivity at high frequency, in this work, $\gamma = 5.75 \times 10^{13} \text{ rad/s}$. $\omega_p^2(\sigma)$ is the angular frequency that varies depending on the electrical conductivity, can be approximately described as $\omega_p^2(\sigma) = \frac{\sigma}{\epsilon_0} \omega_p^2(\sigma_0)$, $\omega_p^2(\sigma) = \frac{ne^2}{\epsilon_0 m^*}$, in which $\sigma_0 = 3 \times 10^5 \text{ S/m}$, $\omega_p(\sigma) = 1.4 \times 10^{15} \text{ rad/s}$, m^* is the effective mass, the carrier concentration is n . VO_2 is modeled as a material with a conductivity of 200 S/m in the insulating state, and that with a conductivity of $2 \times 10^5 \text{ S/m}$ in the metallic state.

3. Results and Discussions

3.1. Electromagnetically Induced Transparency with VO_2 in the Insulating State

When VO_2 is in the insulating state, the device exhibits plasma-induced transparency, which can provide the basis for plasma sensing and symmetrical matching devices. When the conductivity of VO_2 is 200 S/m , terahertz wave normally incident through the VO_2 layer. The top Z-shaped enantiomeric meta-atom interacts with the bottom symmetric Z structure, presenting the characteristic of electromagnetically induced transparency, as shown in Figure 2. A sharp and large transmission window occurs at 0.458 THz , and the

resonance dips of this structure are at 0.322 and 0.546 THz, respectively. At the same time, a small resonant dip and peak appear at 0.133 and 0.148 THz.

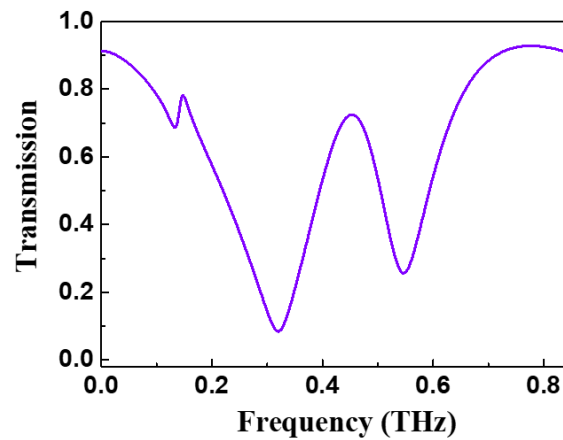


Figure 2. Under TE wave incidence, Characteristic curve of electromagnetically induced transparency when VO₂ is in the insulating state.

To get more insight into the physical origin of the characteristic curve, the surface current distributions of the proposed structures are analyzed. The single top Z structure exhibits a transmission resonance peak at 0.252 THz, and the single bottom one exhibits a resonance peak at 0.228 THz. The corresponding surface current distributions are shown in Figure 3a,b. The integrated distribution at 0.133 THz is shown in Figure 3c, the surface current direction of the bottom symmetric Z structure has little difference from the distribution in Figure 3b. However, the surface current direction of the top Z structure is obviously opposite to that of Figure 3a. After coupling, the surface current directions of the top and bottom Z-shaped enantiomeric structure are the same. The dipole-like oscillations of the enantiomer structure are enhanced by changing the surface current direction of the top Z structure, resulting in a small resonance dip. The surface current distribution at 0.148 THz is shown in Figure 3d, the surface current direction of the top Z structure is the same as that before coupling, while the surface current direction of the bottom symmetric Z structure is totally opposite. The change of the bottom metal structure enhances the electric dipole resonance of the top Z structure. However, the transmission of the whole structure increased by of the surface current intensity decreased, resulting in a small resonant peak in the characteristic curve. At a frequency of 0.322 THz, both the top and bottom Z structures resonate in the direction before coupling. The integrated structure generates a strong current distribution on the surface of the structure as shown in Figure 3e, resulting in a large resonance slope of 0.322 THz. At the frequency of 0.458 THz. The current is concentrated at the transverse bar of the Z-metal and forms a current cycle that produces a strong magnetic dipole in the dielectric layer [46]. We can find that in Figure 3f, the electric dipole and a magnetic dipole are formed at the same time, which lead to the transmissibility of the structure enhanced at 0.458 THz, forming an electromagnetic induced transparency peak. As the incident light band increases, it can be found that the magnetic dipoles in the dielectric layer gradually disappear, and the top and bottom Z structures continue to resonate in the direction before strong coupling. As shown in Figure 3g, a strong current distribution is generated on the surface of the underlying structure at a frequency of 0.546 THz, which also results in a large resonance slope.

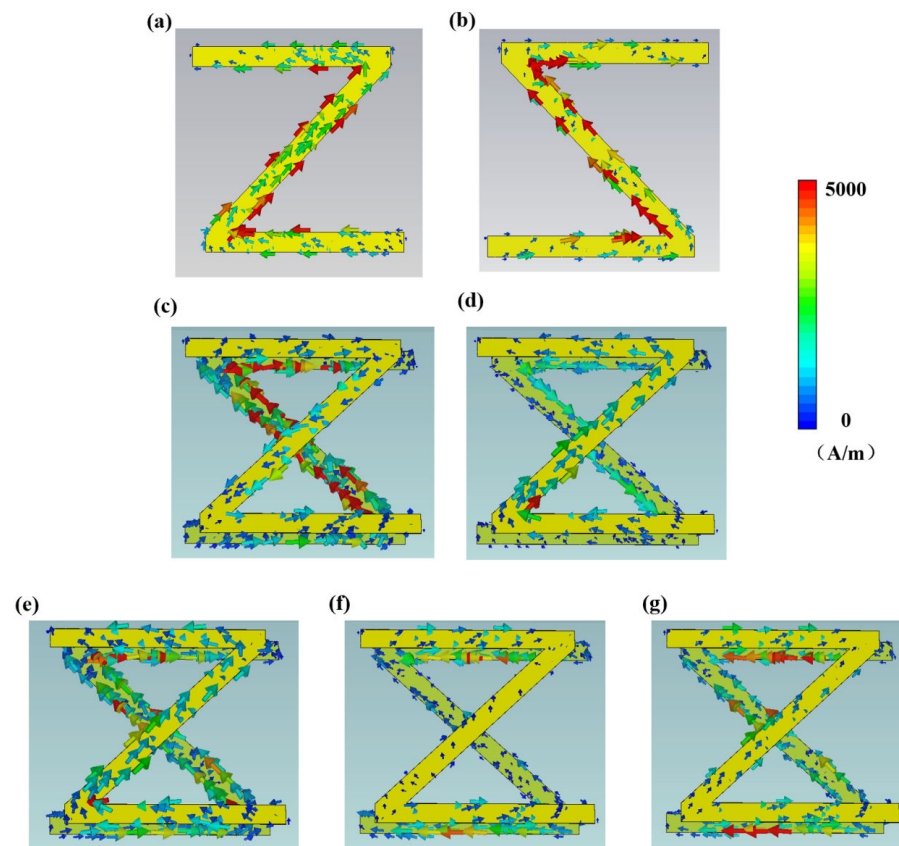


Figure 3. Surface current distributions of the proposed structures. (a) Single top Z-shaped meta-atom. (b) Bottom symmetric Z structure. (c–g) Integrated metasurface at 0.133, 0.148, 0.322, 0.458 and 0.546 THz, respectively.

3.2. Narrow-Band Absorption with VO_2 in the Metallic State

In recent years, metamaterial absorber has attracted great attention. In this design, the top gold Z-shaped meta-atom, the middle SiO_2 spacer, and the bottom VO_2 film formed a typical metallic pattern-insulator-metallic film configuration when VO_2 is in the metallic state. The absorptance can be obtained by $A(\omega) = 1 - R(\omega) - T(\omega) = 1 - |S_{11}|^2 - |S_{21}|^2$, where $A(\omega)$, $R(\omega)$ and $T(\omega)$ are absorptance, reflectance and transmittance, respectively. Due to the conductivity of VO_2 set as 2×10^5 S/m in the metallic state, the transmittance $T(\omega)$ is about 0. Therefore, the absorptance is simplified as $A(\omega) = 1 - |S_{11}|^2$. This designed narrow-band absorber has a near-perfect absorption peak located at 0.525 THz with absorptance of 91%, as shown in Figure 4.

In order to analyze the physical mechanism of the absorber, the effective impedance is calculated by the formula $z = \frac{z_1}{z_0} = \sqrt{\frac{\mu(\omega)}{\varepsilon(\omega)}} = \sqrt{\frac{(1+S_{11}^2)-S_{21}^2}{(1-S_{11}^2)-S_{21}^2}}$, where z_1 is the impedance of the absorber, z_0 is the impedance of the free space, $\mu(\omega)$ is the effective permeability, $\varepsilon(\omega)$ is the effective permittivity and S is the S parameter [47]. The effective impedance will change with permittivity and permeability values. When the permittivity is equal to the permeability, that is $z = 1$, the impedance of the absorber is equal to the impedance of the free space, indicating that the impedance of the absorber and the free space are perfectly matched. The distribution of impedance z is obtained according to the calculation, as shown in Figure 5a,b. The real part of the device impedance is close to 1 and the imaginary part is close to 0 at normal incidence. It is confirmed that the device achieves nearly perfect absorption at 0.525 THz.

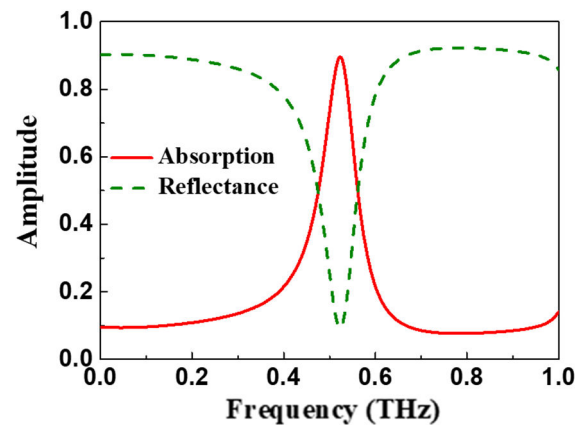


Figure 4. Simulated reflectance and absorptance of the designed system at normal incidence when VO₂ is in the metallic state.

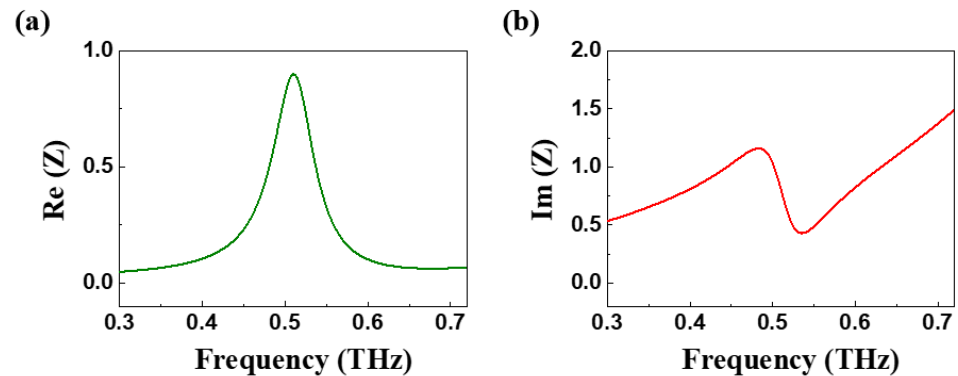


Figure 5. (a) The real part and (b) the imaginary part of the relative impedance of the device when the VO₂ conductivity is 2×10^5 S/m.

The electric field and surface current distribution on the surface of Z-shaped meta-atom and VO₂ layer were analyzed, as shown in Figure 6. At the frequency of 0.525 THz, the positive and negative electric field centers of the Z-shaped meta-atom had the same intensity. The electric field is distributed on both sides of each metal strip, showing strong electric dipole resonance, as shown in Figure 6a. The corresponding electric field on the surface of VO₂ film was calculated at the same time, as shown in Figure 6b. This electric field distribution is caused by the antiparallel electric field distribution. The antiparallel resonance generated an electric dipole moment between the top Z-shaped meta-atom and bottom VO₂ film. It interacted strongly with incident terahertz waves, resulting in a perfect absorption peak at 0.525 THz. Figure 6c shows that the current is directed from one end to the other. The current intensity is concentrated in the center of the three parts of the Z-shaped meta-atom and does not form a current loop. This phenomenon further indicates that the resonance of Z-shaped metal absorber is caused by electric dipole resonance.

The absorption spectra of the absorber with different polarization angles for TM and TE polarization are calculated at normal incident. At TM polarization, the absorptance is relatively high with the polarization angle of 0–60°, as shown in Figure 7a. When the polarization angle is greater than 60°, the absorptance decreases gradually. At TE polarization, the absorptance is almost zero when the polarization angle is 0°. When the angle is greater than 60°, the absorption rate increases gradually as shown in Figure 7b. When the polarization angle is 0°, the electric field of the absorber is effectively excited by electromagnetic field parallel to the TM. When the polarization angle is greater than 60°, the parallel component of the electromagnetic weaken, resulting in a weak coupling between the electromagnetic field and the metasurface. When the polarization angle gradually changes to 90°, the electric dipole resonance is fully excited by electromagnetic waves

parallel to the TE polarization, realizing the change of absorptance from TM mode to TE mode. When the polarization angle gradually increases to 90° , the electric dipole resonance is fully excited by electromagnetic waves parallel to the direction of TE polarization, realizing the change from TM mode to TE mode.

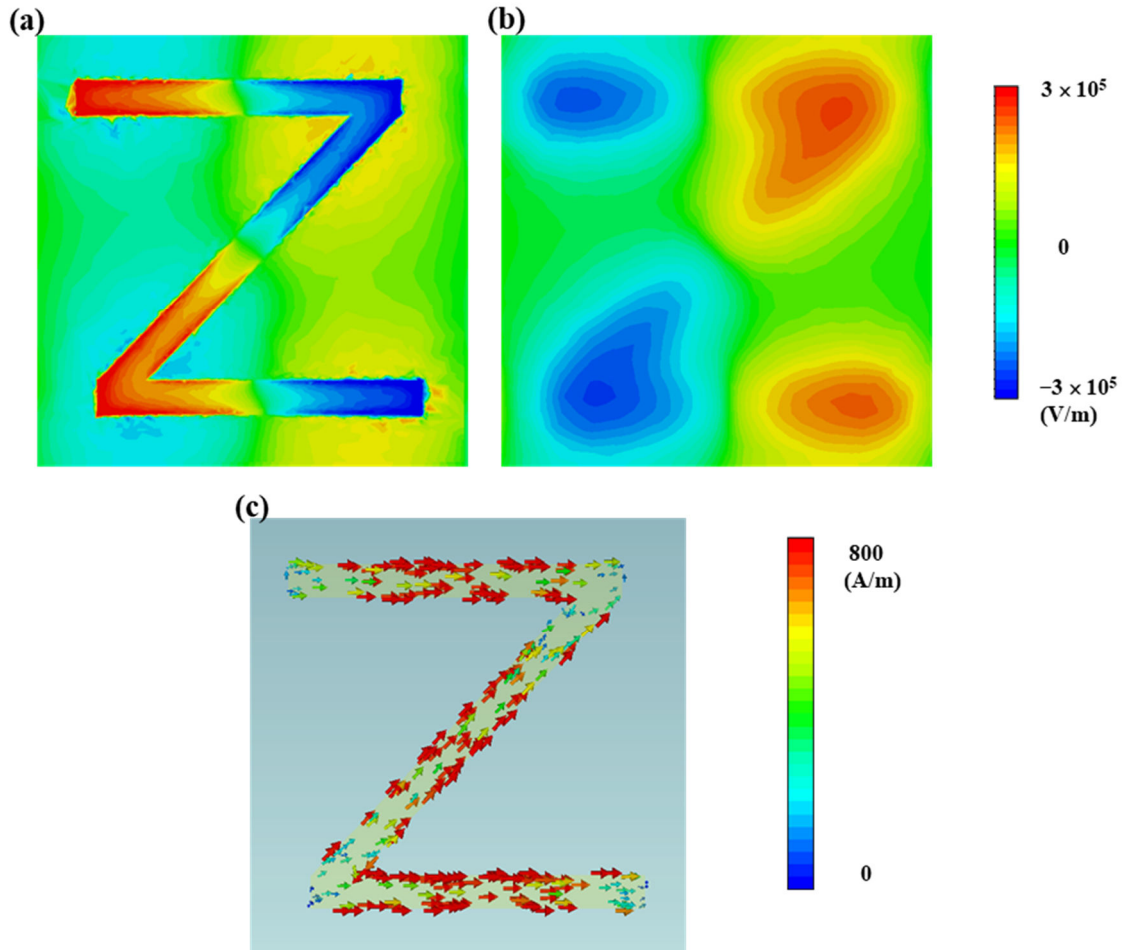


Figure 6. Electric field and surface current distribution of Z-type absorber at 0.525 THz. (a) Electric field distribution on the surface of Z-shaped meta-atom; (b) Electric field distribution on the surface of VO_2 layer; (c) Current distribution on the surface of Z-shaped meta-atom.

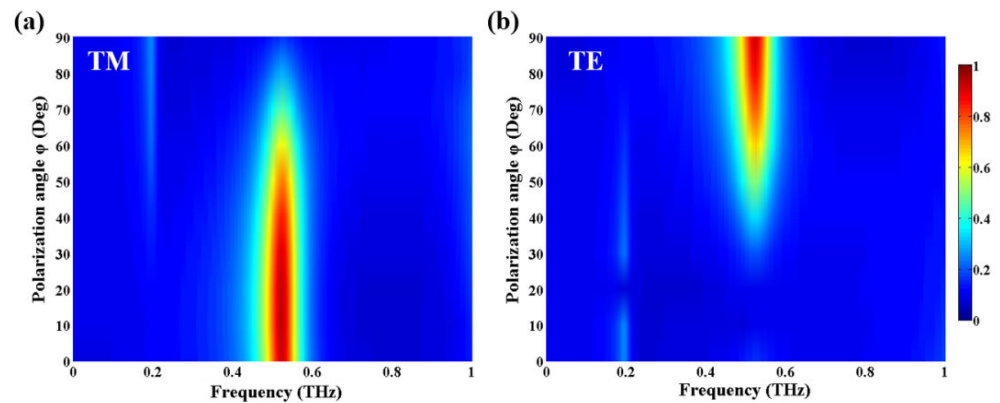


Figure 7. Absorption spectra of the absorber with different polarization angles at 0.525 THz for (a) TM polarization, (b) TE polarization.

In practice, perfect ideal plane waves rarely exist. The direction of the incident terahertz wave is random. Therefore, the influences of different incident angles on the

absorption performance are further discussed in Figure 8. For TM polarization incidence, as shown in Figure 8a, the absorptance maintains stability with the incidence angle. The structure exhibits great absorptance in the range of 0–80°. It is shown that the electromagnetic field is continuously and effectively confined in the dielectric layer with the increase of the incidence angle. Therefore, the absorber is not sensitive to the polarization angle. For TE polarization incidence, as shown in Figure 8b, the absorber has almost no absorption. The results show that the absorber is insensitive to TE and TM polarization in a wide range of incident angles, which indicates that the metasurface has strong practicability.

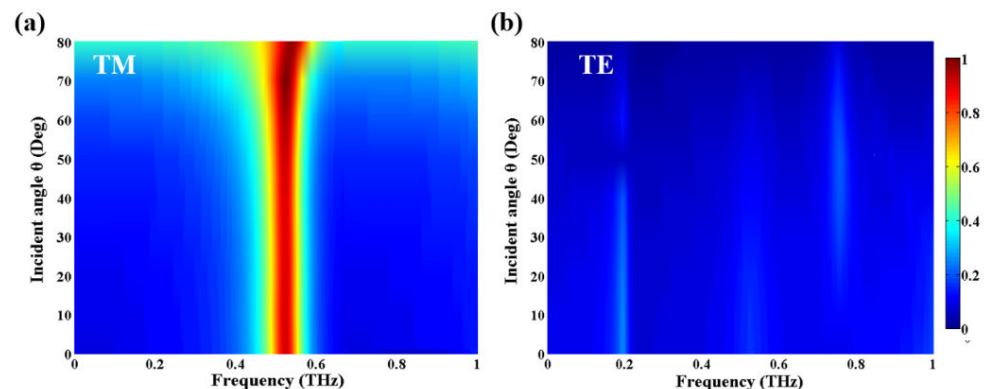


Figure 8. Absorption spectra of the absorber with different incident angles for (a) TM polarization, (b) TE polarization.

4. Conclusions

In conclusion, a switchable bifunctional metasurface with efficient terahertz absorption and electromagnetically induced transparency is proposed and studied. The cell structure of the device combines the double-layer Z-shaped meta-atoms with the VO₂ film at the bottom to achieve flexible switching between the two states. When VO₂ is in the insulating state and transparent to terahertz wave, the analysis shows that the electromagnetically induced transparency is caused by the coupling effect between the double-layer Z-shaped structure. The coupling effect excites second-order dark mode resonance modes and generates effective magnetic dipole oscillations in the dielectric layer. The electric dipole and the magnetic dipole work together, and the metasurface forms an electromagnetically induced transparency peak at 0.458 THz (the maximum transmittance reaches 80%). The distribution of electric and magnetic fields indicates that the broadband EIT effect is the mismatch and hybridization of two coupled bright modes supported by metasurfaces, realized by frequency. During the VO₂ phase transition with increasing conductivity, the metasurface gradually closes the EIT window and begins to absorb incident terahertz waves. When VO₂ is in a completely metallic state, the component operates as an almost perfect absorber, with a total absorption rate exceeding 91%. On the other hand, broadband near-perfect absorption results from strong excitation and the superposition of two resonances within the MIM cavity. The key geometric parameters that affect the performance of metasurfaces have been studied, further clarifying the design flexibility of metasurfaces. This versatile tunable phase-change device can add value to potential terahertz applications such as intelligent modulators, slow light devices, and imaging coding. The design principles can also be extended to other infrared and optical devices with switchable and diverse functions.

Author Contributions: Conceptualization, H.C. and Y.Y.; methodology, H.C.; software, H.C. and Y.Y.; investigation, H.C., J.Z. and J.L.; resources, L.M. and J.L.; writing—original draft preparation, H.C. and Y.Y.; writing—review and editing, H.C., Y.Y., J.Z. and J.L.; supervision, L.M. and J.L.; writing—review and editing, L.M. and J.L. All authors have read and agreed to the published version of the manuscript.

Funding: This work was supported by National Natural Science Foundation of China No. 62201378; National Key Research and Development Program of China (2018YFE0202500); Guangdong Basic and Applied Basic Research Foundation (No.2020A1515110709).

Institutional Review Board Statement: Not applicable.

Informed Consent Statement: Not applicable.

Data Availability Statement: Data underlying the results presented in this paper are not publicly available at this time but may be obtained from the authors upon reasonable request.

Conflicts of Interest: The authors declare no conflict of interest.

References

1. He, Q.; Sun, S.; Xiao, S.; Zhou, L. High-Efficiency Metasurfaces: Principles, Realizations, and Applications. *Adv. Opt. Mater.* **2018**, *6*, 1800415. [[CrossRef](#)]
2. Nong, J.; Tang, L.; Lan, G.; Luo, P.; Li, Z.; Huang, D.; Yi, J.; Shi, H.; Wei, W. Enhanced Graphene Plasmonic Mode Energy for Highly Sensitive Molecular Fingerprint Retrieval. *Laser Photonics Rev.* **2020**, *15*, 2000300. [[CrossRef](#)]
3. Kotov, O.V.; Lozovik, Y.E. Dielectric response and novel electromagnetic modes in three-dimensional Dirac semimetal films. *Phys. Rev. B* **2016**, *93*, 235417. [[CrossRef](#)]
4. Beruete, M.; Jáuregui-López, I. Terahertz Sensing Based on Metasurfaces. *Adv. Opt. Mater.* **2019**, *8*, 1900721. [[CrossRef](#)]
5. Amin, M.; Khan, A.D. Polarization selective electromagnetic-induced transparency in the disordered plasmonic quasicrystal structure. *J. Phys. Chem. C* **2015**, *119*, 21633–21638. [[CrossRef](#)]
6. Li, J.; Li, J.T.; Yue, Z.; Zheng, C.L.; Wang, G.C.; Liu, J.Y.; Xu, H.; Song, C.Y.; Yang, F.; Li, H.; et al. Structured Vector Field Manipulation of Terahertz Wave along the Propagation Direction Based on Dielectric Metasurfaces. *Laser Photonics Rev.* **2022**, *16*, 2200325. [[CrossRef](#)]
7. Aimal, D.K.; Qandeel, R.; Adnan, D.K.; Fazal, E.S.; Muhammad, N.; Salman, A.; Haseeb, A.K. Broadband Solar Energy Absorption in Plasmonic Thin-Film Amorphous Silicon Solar Cell. *Coatings* **2019**, *9*, 638.
8. Jepsen, P.U.; Fischer, B.M.; Thoman, A.; Helm, H.; Suh, J.Y.; Lopez, R.; Haglund, R.F. Metal-insulator phase transition in a VO₂ thin film observed with terahertz spectroscopy. *Phys. Rev. B* **2006**, *74*, 205103.1–205103.9. [[CrossRef](#)]
9. Nakajima, M.; Takubo, N.; Hiroi, Z.; Ueda, Y.; Suemoto, T.J.A.P.L. Photoinduced metallic state in VO₂ proved by the terahertz pump-probe spectroscopy. *Appl. Phys. Lett.* **2008**, *92*, 6853. [[CrossRef](#)]
10. Qi-Ye, W.; Huai-Wu, Z.; Qing-Hui, Y.; Yun-Song, X.; Kang, C. Terahertz metamaterials with VO₂ cut-wires for thermal tunability. *Appl. Phys. Lett.* **2010**, *97*, 597.
11. Lei, L.; Lou, F.; Tao, K.; Huang, H.; Cheng, X.; Xu, P. Tunable and scalable broadband metamaterial absorber involving VO₂-based phase transition. *Phot. Res.* **2019**, *7*, 734–741. [[CrossRef](#)]
12. Song, Z.; Zhang, J. Achieving broadband absorption and polarization conversion with a vanadium dioxide metasurface in the same terahertz frequencies. *Opt. Express* **2020**, *28*, 12487–12497. [[CrossRef](#)] [[PubMed](#)]
13. Chen, L.; Song, Z. Simultaneous realizations of absorber and transparent conducting metal in a single metamaterial. *Opt. Express* **2020**, *28*, 6565–6571. [[CrossRef](#)] [[PubMed](#)]
14. Song, Z.; Chen, A.; Zhang, J.; Wang, J. Integrated metamaterial with functionalities of absorption and electromagnetically induced transparency. *Opt. Express* **2019**, *27*, 25196–25204. [[CrossRef](#)]
15. Holsteen, A.; Kim, I.S.; Lauhon, L.J.J. Extraordinary Dynamic Mechanical Response of Vanadium Dioxide Nanowires around the Insulator to Metal Phase Transition. *Nano Lett.* **2016**, *14*, 1898–1902. [[CrossRef](#)]
16. Bai, J.; Zhang, S.; Fan, F.; Wang, S.; Chang, S.J. Tunable broadband THz absorber using vanadium dioxide metamaterials. *Opt. Commun.* **2019**, *452*, 292–295. [[CrossRef](#)]
17. Zhang, Y.; Qiao, S.; Sun, L.; Shi, Q.W.; Huang, W.; Li, L.; Yang, Z.J. Photoinduced active terahertz metamaterials with nanostructured vanadium dioxide film deposited by sol-gel method. *Opt. Express* **2014**, *22*, 11070–11078. [[CrossRef](#)]
18. Driscoll, T.; Palit, S.; Qazilbash, M.M.; Brehm, M.; Keilmann, F.; Chae, B.G.; Yun, S.J.; Kim, H.T.; Cho, S.Y.; Jokerst, N.M. Dynamic tuning of an infrared hybrid-metamaterial resonance using vanadium dioxide. *Appl. Phys. Lett.* **2008**, *93*, 18. [[CrossRef](#)]
19. Park, D.J.; Shin, J.H.; Park, K.H.; Ryu, H.C. Electrically controllable THz asymmetric split-loop resonator with an outer square loop based on VO₂. *Opt. Express* **2018**, *26*, 17397–17406. [[CrossRef](#)]
20. Shin, J.H.; Park, K.H.; Ryu, H.C. Electrically controllable terahertz square-loop metamaterial based on VO₂ thin film. *Nanotechnology* **2016**, *27*, 195202. [[CrossRef](#)]
21. Chang, T.; Cao, X.; Li, N.; Long, S.; Zhu, Y.; Huang, J.; Luo, H.; Jin, P. Mitigating Deterioration of Vanadium Dioxide Thermochromic Films by Interfacial Encapsulation. *Matter* **2019**, *1*, 734–744. [[CrossRef](#)]
22. Xu, G.; Jin, P.; Tazawa, M.; Yoshimura, K. Optimization of antireflection coating for VO₂-based energy efficient window. *Sol. Energy Mater. Sol. Cells* **2004**, *83*, 29–37. [[CrossRef](#)]
23. Huang, J.; Li, J.; Yang, Y.; Li, J.; Zhang, Y.; Yao, J. Active controllable dual broadband terahertz absorber based on hybrid metamaterials with vanadium dioxide. *Opt. Express* **2020**, *28*, 7018. [[CrossRef](#)] [[PubMed](#)]

24. Liu, M.; Plum, E.; Li, H.; Duan, S.; Li, S.; Xu, Q.; Zhang, X.; Zhang, C.; Zou, C.; Jin, B.; et al. Switchable Chiral Mirrors. *Adv. Opt. Mater.* **2020**, *8*, 2000247. [[CrossRef](#)]
25. Zhang, Z.; Yang, J.; Han, Y.; He, X.; Zhang, J.; Huang, J.; Chen, D.; Xu, S.; Xie, W. Actively tunable terahertz electromagnetically induced transparency analogue based on vanadium-oxide-assisted metamaterials. *Appl. Phys. A* **2020**, *126*, 199. [[CrossRef](#)]
26. Xiao, S.; Wang, T.; Liu, T.; Zhou, C.; Jiang, X.; Zhang, J. Active metamaterials and metadevices: A review. *J. Phys. D Appl. Phys.* **2020**, *53*, 503002. [[CrossRef](#)]
27. Ding, F.; Zhong, S.; Bozhevolnyi, S.I. Vanadium Dioxide Integrated Metasurfaces with Switchable Functionalities at Terahertz Frequencies. *Adv. Opt. Mater.* **2018**, *6*, 1701204. [[CrossRef](#)]
28. Wang, D.; Sun, S.; Feng, Z.; Tan, W. Enabling switchable and multifunctional terahertz metasurfaces with phase-change material. *Opt. Mater. Express* **2020**, *10*, 2054–2065. [[CrossRef](#)]
29. Agarwal, S.; Srivastava, G.; Prajapati, Y.K. Dual band Vis-IR absorber using bismuth based helical metamaterial surface. *Opt. Quant. Electron.* **2022**, *54*, 772. [[CrossRef](#)]
30. Agarwal, S.; Prajapati, Y.K. Design of broadband absorber using 2D materials for thermo-photovoltaic cell application. *Opt. Commun.* **2018**, *413*, 39–43. [[CrossRef](#)]
31. Agarwal, S.; Prajapati, Y.K. Metamaterial based sucrose detection sensor using transmission spectroscopy. *Optik* **2020**, *205*, 164276. [[CrossRef](#)]
32. Agarwal, S. Multifunctional metamaterial surface for absorbing and sensing applications. *Opt. Commun.* **2019**, *439*, 304–307. [[CrossRef](#)]
33. Mpa, B.; Glc, D.; Ab, A.; Ms, E. Photochemical degradation of the environmental pollutants over the worm-like $\text{Nd}_2\text{CuO}_4/\text{Nd}_2\text{O}_3$ nanostructures. *Nano-Struct. Nano-Objects* **2019**, *18*, 100258.
34. Padervand, B. One-pot synthesis of novel ternary $\text{Fe}_3\text{N}/\text{Fe}_2\text{O}_3/\text{C}_3\text{N}_4$ photocatalyst for efficient removal of rhodamine B and CO_2 reduction. *J. Alloy. Compd.* **2021**, *852*, 156955. [[CrossRef](#)]
35. Gao, T.; Lin, J.; Zhang, K.; Padervand, M.; Zhang, Y.; Zhang, W.; Shi, M.; Wang, C. Porous Defective Bi/ Bi_3NbO_7 Nanosheets for Efficient Photocatalytic NO Removal under Visible Light. *Processes* **2023**, *11*, 115. [[CrossRef](#)]
36. Montaser, A.M. Design of metamaterial absorber for all bands from microwave to terahertz ranges. *Int. J. Adv. Res. Electron. Commun. Eng.* **2016**, *5*, 1475–1481.
37. Jang, T.; Youn, H.; Shin, Y.J.; Guo, L.J. Transparent and flexible polarization-independent microwave broadband absorber. *ACS Photonics* **2014**, *1*, 279–284. [[CrossRef](#)]
38. Wu, B.; Tuncer, H.M.; Naem, M.; Yang, B.; Cole, M.T.; Milne, W.I.; Hao, Y. Experimental demonstration of a transparent graphene millimetre wave absorber with 28% fractional bandwidth at 140 GHz. *Sci. Rep.* **2014**, *4*, 4130. [[CrossRef](#)]
39. Batrakov, K.; Kuzhir, P.; Maksimenko, S.; Paddubskaya, A.; Voronovich, S.; Lambin, P.; Kaplas, T.; Svirko, Y. Flexible transparent graphene/polymer multilayers for efficient electromagnetic field absorption. *Sci. Rep.* **2014**, *4*, 7191. [[CrossRef](#)]
40. Jung, H.; Jo, H.; Lee, W.; Kim, B.; Choi, H.; Kang, M.S.; Lee, H. Electrical control of electromagnetically induced transparency by terahertz metamaterial funneling. *Adv. Opt. Mater.* **2019**, *7*, 1801205. [[CrossRef](#)]
41. Zhao, Z.; Zhao, H.; Ako, R.T.; Zhang, J.; Zhao, H.; Sriram, S. Demonstration of group delay above 40 ps at terahertz plasmon-induced transparency windows. *Opt. Express* **2019**, *27*, 26459. [[CrossRef](#)] [[PubMed](#)]
42. Yahiaoui, R.; Burrow, J.A.; Mekonen, S.M.; Sarangan, A.; Mathews, J.; Agha, I.; Searles, T.A. Electromagnetically induced transparency control in terahertz metasurfaces based on bright-bright mode coupling. *Phys. Rev. B* **2018**, *97*, 155403. [[CrossRef](#)]
43. Hu, J.; Lang, T.; Hong, Z.; Shen, C.; Shi, G. Comparison of electromagnetically induced transparency performance in metallic and all-dielectric metamaterials. *J. Light. Technol.* **2018**, *36*, 2083–2093. [[CrossRef](#)]
44. Wang, S.; Cai, C.; You, M.; Liu, F.; Werner, D.H. Vanadium dioxide based broadband THz metamaterial absorbers with high tunability: Simulation study. *Opt. Express* **2019**, *27*, 19436. [[CrossRef](#)] [[PubMed](#)]
45. Song, Z.; Chen, A.; Zhang, J. Terahertz switching between broadband absorption and narrowband absorption. *Opt. Express* **2020**, *28*, 2037–2044. [[CrossRef](#)] [[PubMed](#)]
46. Bochkova, E.; Burokur, S.N.; De Lustrac, A.; Lupu, A. Direct dark modes excitation in bi-layered enantiomeric atoms-based metasurface through symmetry matching. *Opt. Lett.* **2016**, *41*, 412–415. [[CrossRef](#)] [[PubMed](#)]
47. Huang, J.; Li, J.; Yang, Y.; Li, J.; Li, J.; Zhang, Y.; Yao, J. Broadband terahertz absorber with a flexible, reconfigurable performance based on hybrid-patterned vanadium dioxide metasurfaces. *Opt. Express* **2020**, *28*, 17832–17840. [[CrossRef](#)] [[PubMed](#)]

Disclaimer/Publisher’s Note: The statements, opinions and data contained in all publications are solely those of the individual author(s) and contributor(s) and not of MDPI and/or the editor(s). MDPI and/or the editor(s) disclaim responsibility for any injury to people or property resulting from any ideas, methods, instructions or products referred to in the content.